

Hard X-ray observation and multiwavelength study of the PeVatron candidate pulsar wind nebula “Dragonfly”

JOOYUN WOO ¹, HONGJUN AN ², JOSEPH D. GELFAND ³, CHARLES J. HAILEY ¹, KAYA MORI ¹,
RESHMI MUKHERJEE ⁴, SAMAR SAFI-HARB ⁵, AND TEA TEMIM ⁶

¹*Columbia Astrophysics Laboratory, 550 West 120th Street, New York, NY 10027, USA*

²*Department of Astronomy and Space Science, Chungbuk National University, Cheongju, 28644, Republic of Korea*

³*NYU Abu Dhabi, PO Box 129188, Abu Dhabi, United Arab Emirates*

⁴*Department of Physics and Astronomy, Barnard College, 3009 Broadway, New York, NY 10027, USA*

⁵*Department of Physics and Astronomy, University of Manitoba, Winnipeg, MB R3T 2N2, Canada*

⁶*Princeton University, 4 Ivy Ln, Princeton, NJ 08544, USA*

ABSTRACT

We studied the PeVatron nature of the pulsar wind nebula G75.2+0.1 (“Dragonfly”) as part of our *NuSTAR* observational campaign of energetic PWNe. The Dragonfly is spatially coincident with LHAASO J2018+3651 whose maximum photon energy is 0.27 PeV. We detected a compact (radius 1′) inner nebula of the Dragonfly without a spectral break in 3 – 20 keV using *NuSTAR*. A joint analysis of the inner nebula with the archival *Chandra* and XMM-Newton observations yields a power-law spectrum with $\Gamma = 1.49 \pm 0.03$. Synchrotron burnoff is observed from the shrinkage of the NuSTAR nebula at higher energies, from which we infer the magnetic field in the inner nebula of 24 μ G at 3.5 kpc. Our analysis of archival XMM data and 13 years of *Fermi*-LAT data confirms the detection of an extended ($\sim 10'$) outer nebula in 2 – 6 keV ($\Gamma = 1.82 \pm 0.03$) and non-detection of a GeV nebula, respectively. Using the VLA, XMM, and HAWC data, we modeled a multi-wavelength spectral energy distribution of the Dragonfly as a leptonic PeVatron. The maximum injected particle energy of 1.4 PeV from our model suggests that the Dragonfly is likely a PeVatron. Our model prediction of the low magnetic field (2.7 μ G) in the outer nebula and recent interaction with the host supernova remnant’s reverse shock (4 kyrs ago) align with common features of PeVatron PWNe. The origin of its highly asymmetric morphology, pulsar proper motion, PWN-SNR interaction, and source distance will require further investigations in the future including a multi-wavelength study using radio, X-ray, and gamma-ray observations.

1. INTRODUCTION

Pulsar wind nebulae (PWNe) of energetic (spin-down luminosity $\dot{E} > 10^{36}$ erg/s) middle-aged (characteristic age $\tau = 10 - 100$ kyr) pulsars are often associated with very-high-energy (VHE, above 1 TeV) sources (e.g., H.E.S.S. Collaboration et al. (2018)). Many of them are luminous above a hundred TeV without a hint of a spectral cutoff (e.g., Abeysekara et al. (2020) and Sudoh et al. (2021)). Recently, the higher energy regime of their spectra was unveiled by the Large High Altitude Air Shower Observatory (LHAASO), the first gamma-ray observatory sensitive to PeV-energy gamma rays,

and their detection of 14 Galactic ultra-high-energy (UHE, above 100 TeV) sources (Cao et al. (2021a), Aharonian et al. (2021), and Cao et al. (2021b)). The highest photon energies detected from these sources range from several hundred TeV to above 1 PeV: irrefutable evidence of particle acceleration above 1 PeV in both hadronic (neutral pion decay) and leptonic (inverse Compton scattering) cases. Identifying these Galactic “PeVatrons” is the key to the origin of the highest-energy Galactic cosmic rays observed on the Earth (in hadronic case) as well as a better understanding of the particle acceleration, radiation, and transportation mechanism (in both hadronic and leptonic case).

The majority of the LHAASO sources are spatially coincident with middle-aged energetic PWNe, well-known leptonic particle accelerators. Our *NuSTAR* observational campaign of energetic PWNe aims to explore

the extreme nature of such PWNe (Mori et al. (2022)). Broadband hard X-ray observations with *NuSTAR* provide a unique window to the highest end of their parent particle spectra by resolving their synchrotron radiation without contamination from thermal radiation. Combined with modeling the multi-wavelength (MW) spectral energy distribution (SED) of the PWNe over 20 decades of energy range, it allows deducing the key physical parameters that define the systems, such as the maximum particle energy and magnetic field. Our *NuSTAR* observation and MW SED modeling have functioned as powerful probes of PWNe as energetic leptonic cosmic ray accelerators in our Galaxy (e.g., Burgess et al. (2022), Park et al. (2023a), and Park et al. (2023b)).

G75.2+0.1 (“Dragonfly”) is one of the eight target PWNe of our *NuSTAR* observational campaign and is likely associated with LHAASO J2018+3651. The Dragonfly is powered by PSR J2021+3651 (RA = 20:21:05.40, Dec = +36:51:04.5) first discovered by Roberts et al. (2002) as a radio pulsar with a rotation period $P \cong 104$ ms. The radio observation of the pulsar was motivated by the detection of an unidentified X-ray source AX J2021.1+3651 (Roberts et al. (2001)), which was a follow-up observation of an unidentified gamma-ray source GeV J2020+3658 (Hartman et al. (1999)). As a middle-aged pulsar whose characteristic age $\tau \equiv P/2\dot{P} \sim 17$ kyr, PSR J2021+3651 is still energetic, with $\dot{E} \sim 3.4 \times 10^{36}$ erg s $^{-1}$. PSR J2021+3651 is detected in X-ray as a soft (mostly) thermal ($kT_{BB} = 0.16 \pm 0.02$ keV) point source by *Chandra* (Hessels et al. (2004) and Van Etten et al. (2008)). The authors of both works reported the detection of X-ray pulsations to be insignificant. The PWN G75.2+0.1 of PSR J2021+3651 was first observed in X-ray by Hessels et al. (2004) and was named the “Dragonfly” by Van Etten et al. (2008) for its double-torus structure. *Fermi*-LAT (*Fermi*) observation by (Abdo et al. (2009)) detected GeV pulsations from PSR J2021+3651, yet its spectrum sharply cuts off below 10 GeV with no evidence of higher energy emission from the PWN.

PSR J2021+3651 and the Dragonfly are located in the Cygnus region, an active star-forming region. The first TeV gamma-ray source detected in spatial coincidence with PSR J2021+3651 and the Dragonfly was MGRO J2019+37 (Abdo et al. (2007)). MGRO J2019+37 is the second brightest TeV source in the northern hemisphere after the Crab Nebula and largely extended (circular 2D Gaussian with $\sigma = 0.32^\circ \pm 0.12^\circ$). Since its detection, numerous observations in different wavebands have been carried out as attempts to identify the origin of such high energy emissions. Roberts et al. (2008) observed the region with the VLA in radio (20 cm)

and the XMM-Newton (XMM) in soft X-rays. Both observations revealed a more comprehensive picture of G75.2+0.1 beyond the substructures seen by *Chandra* – a conical diffuse nebula pivoted at PSR J2021+3651 that extends out to $\sim 20'$ (radio) and $\sim 10'$ (soft X-ray) on the west with decreasing surface brightness. In this work, the entire structure of the PWN is referred to as the Dragonfly.

Aliu et al. (2014) used the Very Energetic Radiation Imaging Telescope Array System (VERITAS) to resolve MGRO J2019+37 into two separate sources: VER J2019+368 and VER J2016+371. While VER J2016+371 is dominated by low-energy (below 1 TeV) emission near a supernova remnant (SNR) CTB 87, VER J2019+368 (RA = 20:19:25, Dec = 36:48:14, elliptical 2D Gaussian with major-axis $\sigma_{maj} = 0.34^\circ \pm 0.03^\circ$ and minor-axis $\sigma_{min} = 0.13^\circ \pm 0.02^\circ$) is bright above 1 TeV. With additional 120 hours of data, Abeysekara et al. (2018) reported that VER J2019+368 may be resolved into two source candidates, VER J2020+368* and VER J2018+367*. The High-Altitude Water Cherenkov gamma-ray observatory (HAWC) found the high-energy emission from VER J2019+368 to be significant even above 56 TeV and named the source eHWC J2019+368 (Abeysekara et al. (2020)). Its significant detection above 100 TeV by LHAASO with the maximum photon energy 0.27 ± 0.02 PeV (Cao et al. (2021a)) confirms that one or more PeVatrons of Galactic origin are present in this region. This extreme Galactic source, namely LHAASO J2018+3651, is spatially coincident with multiple possible cosmic ray accelerators, including a Wolf-Rayet (WR) star WR 141, H II region Sh 2-104, PSR J2021+3651 and the Dragonfly.

In this work, we aim to evaluate the Dragonfly’s potential as a leptonic PeVatron. We report the first hard X-ray observation of the Dragonfly using *NuSTAR*. We analyze the archival *Chandra* and XMM data and 13 years of *Fermi* data on the Dragonfly. We combine the spectra of the Dragonfly extracted from our analyses with the radio and TeV spectra from the previous works to model the MW SED of the Dragonfly. We discuss the common features of PeVatron PWNe, source distance, and magnetic field.

2. X-RAY DATA ANALYSIS

We analyzed two sets of archival *Chandra* data (Obs ID 8502, 34 ks, 2006 Dec 25, and Obs ID 7603, 60 ks, 2006 Dec 29), one set of archival XMM data (Obs ID 0674050101, 135 ks, 2012 Apr 17), one set of new *NuSTAR* data (Obs ID 40660004002, 61 ks, 2021 May 19). We processed the *Chandra* data using the `chandra_repro` task in CIAO 4.13 (Fr-

uscione et al. (2006)) and the calibration database CALDB 4.9.5. We processed *NuSTAR* data using the `nuproducts` task in *NuSTAR* Data Analysis Software package (NuSTARDAS v2.0.0) contained within HEASOFT 6.28 and the *NuSTAR* calibration database (CALDB version 20210315). We processed the XMM European Photon Imaging Camera (EPIC) MOS data using the `emchain` and `emfilter` tasks in the XMM-Newton Extended Source Analysis Software (XMM-ESAS) package contained within the XMM-Newton Science Analysis System (SAS v20.0.0). The net exposure after removing soft proton (SP) flares is 85 ks. The XMM EPIC pn data was not used since it was obtained in small window mode (one single CCD) and hence is inappropriate for observing a large diffuse nebula that extends over multiple CCDs.

2.1. Timing analysis

Hessels et al. (2004) reported a marginal (3.7σ) detection of X-ray pulsations in 0.5 – 3 keV from PSR J2021+3651 using a *Chandra* data in continuous-clocking mode and contemporaneous radio ephemeris. The same authors reported significant timing noise and a possibility of large glitches in PSR J2021+3651. We attempted to search for hard X-ray pulsations from PSR J2021+3651 using the *NuSTAR* data. We applied an astrometric correction on the pulsar position to the cleaned event files using the *Chandra* data analyzed in this work. We applied a barycentric correction to these event files for the corrected pulsar position using the `barycorr` task in NuSTARDAS. We used `extractor` to select position- and timing-corrected events within the $r = 30''$ circular region around PSR J2021+3651 corresponding to the half-power diameter (HPD) of *NuSTAR*. We generated binned light curves from the selected events in 3 – 6, 6 – 20, and 3 – 20 keV bands (bin size = 1 ms) using the timing analysis software HENDRICS 7.0 (Bachetti (2018)). We used the light curves to create power spectra with the timing analysis software Stingray v1.1 (Huppenkothen et al. (2019)). No significant frequency features were found. Given the lack of contemporaneous pulsar ephemeris, we performed Z_n^2 ($n = 2$) searches around the radio pulsar frequency and frequency derivative found by Roberts et al. (2002). This search did not yield a significant detection of pulsations.

2.2. Imaging analysis

Van Etten et al. (2008) resolved the substructures of the PSR J2021+3651 and the Dragonfly using *Chandra*. Such substructures include pulsar jets, $20'' \times 10''$ double-torus inner nebula, a bow shock standoff, and a

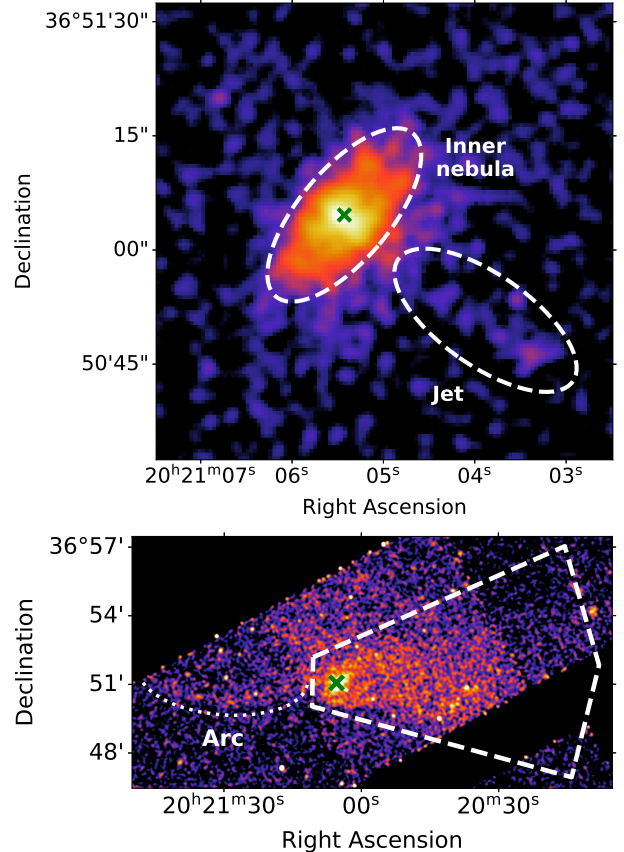


Figure 1. Merged (Obs ID 8502 and 7603) and exposure-corrected *Chandra* images of the Dragonfly in 2 – 6 keV. The scales were adjusted for better legibility. PSR J2021+3651 is marked as a cross (X) in both images. *Top:* $1' \times 1'$ image after Gaussian smoothing with $\sigma = 1.5$ pixel = $0.7''$. The $20'' \times 10''$ inner nebula and the pulsar jet stretching out to $\sim 30''$ from the pulsar are marked with dashed lines. *Bottom:* $21' \times 11'$ image after Gaussian smoothing with $\sigma = 3$ pixel = $3.0''$. The arc in length $\sim 7.7'$ is traced with a dotted line. The extent of the outer nebula seen by XMM is marked as a dashed line.

peculiar “arc” stretching toward the east of the pulsar (dotted line in the bottom figure of Figure 1). An outer nebula with a size much larger than the inner nebula seen by *Chandra* was discovered by Roberts et al. (2008) using XMM. Zabalza et al. (2010) used XMM observations covering the region further west to that of Roberts et al. (2008) and constrained the size of the outer nebula to 10 – 15' to the west of PSR J2021+3651. Mizuno et al. (2017) not only confirmed the western extent of the outer nebula measured by Zabalza et al. (2010) using Suzaku but also claimed the emission seen by XMM on the east of PSR J2021+3651 including the “arc” is part of the outer nebula.

In this section, we discuss the X-ray morphology of the Dragonfly seen by *Chandra*, XMM, and *NuSTAR*.

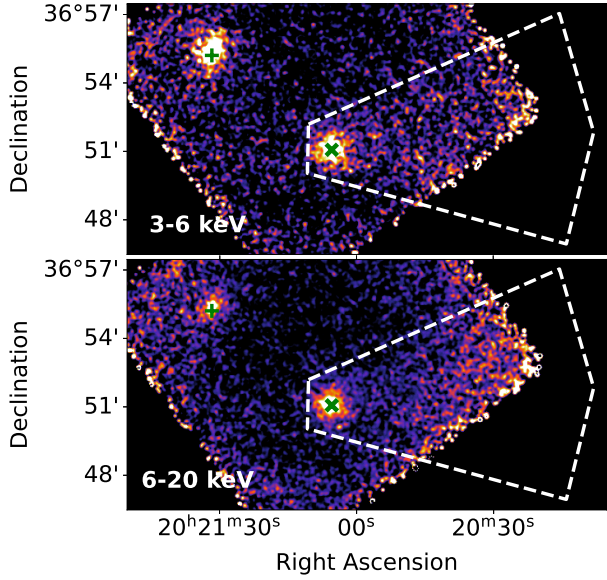


Figure 2. Merged (FPMA and FPMB) and exposure- and vignetting-corrected $21' \times 11'$ *NuSTAR* images after Gaussian smoothing with $\sigma = 1.5$ pixels = $4.7''$. The scales were adjusted for better legibility. PSR J2021+3651 and WR 141 are marked with a cross (X) and a plus (+), respectively. The extent of the outer nebula seen by XMM is marked with a dashed line.

We investigate a change in the morphology of the hard X-ray nebula in two different energy ranges: soft band (3 – 6 keV) and hard band (6 – 20 keV). We present the XMM image of the Dragonfly to study the morphology of the outer nebula and briefly discuss the nature of the “arc.” *Chandra* images in 2 – 6 keV are compared to the *NuSTAR* and XMM images in similar energy ranges (3 – 6 keV and 2 – 6 keV, respectively). A detailed description of the *Chandra* image can be found in [Van Etten et al. \(2008\)](#).

2.2.1. *Chandra* image

We merged the two *Chandra* observations (Obs ID 8502 and 7603) using the `merge_obs` task in CIAO to create an exposure-corrected image in 2 – 6 keV.

Figure 1 shows smaller (inner nebula and jet) and larger (outer nebula and arc) structures of the Dragonfly. The inner nebula is centered at PSR J2021+3651 and axis-symmetric along the jet. Its size is $20''$ along the major axis and $10''$ along the minor axis in diameter. The jet is measured to extend out to $30''$ from the pulsar. The observations covered only part of the outer nebula seen by XMM (dashed line in the bottom panel of Figure 1), yet it is clearly visible. The arc continues to the edge of the FOV, measuring $7.7'$ in length.

2.2.2. *NuSTAR* image

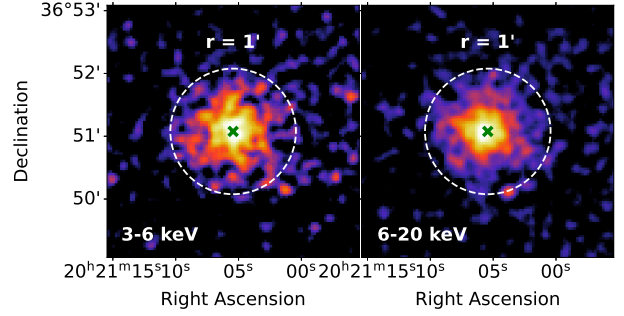


Figure 3. $4' \times 4'$ *NuSTAR* images of the inner nebula. The images were created following the same procedures described in the caption of Figure 2. PSR J2021+3651 is marked with a cross (X). A dashed circle of radius $1'$ is shown as a reference.

We created images for both focal plane modules (FPMA and FPMB) in the soft band (3 – 6 keV) and the hard band (6 – 20 keV) using `extractor`. The corresponding exposure maps after vignetting correction were created using `nuexpomap` task in NuSTARDAS. We combined the FPMA and FPMB images and corrected the exposure using `XIMAGE` to create Figure 2.

A bright emission is detected in both energy bands at the location of PSR J2021+3651 (marked with a cross (X) in the figure) and the surrounding region (inner nebula). The west of PSR J2021+3651 is contaminated by a stray light background, so it is difficult to estimate the emission from the faint outer nebula. WR 141 (marked with a plus sign (+) in the figure) becomes significantly dimmer in the hard band. To examine the detailed morphology of the inner nebula, we created zoomed-in images (Figure 3). The emission is roughly symmetric about the pulsar in both energy bands. The nebula fits well in a radius $1'$ circle, while it shows an apparent decrease in size in the hard band (6 – 20 keV). We fitted PSF-convolved models to the images using `Sherpa` ([Freeman et al. \(2001\)](#)), a fitting and modeling application in CIAO. Both images are fitted with a constant background and a single 2D Gaussian. The FWHM of the Gaussian is $26.5'' \pm 3.2''$ for the soft band and $15.2'' \pm 2.0''$ for the hard band.

2.2.3. *XMM* image

XMM is the only instrument whose image captures the entirety of the outer nebula in the X-ray band. To study this large diffuse emission, we first removed the contamination of the outer nebula by bright point sources in the FOV, such as PSR J2021+3651, WR 141, and a star USNO-B1.0 1268-0448692. We created Swiss cheese masks for MOS1 and MOS2 images that reduce the surface brightness of point sources to 20% of the surrounding background using the `cheese` task. These

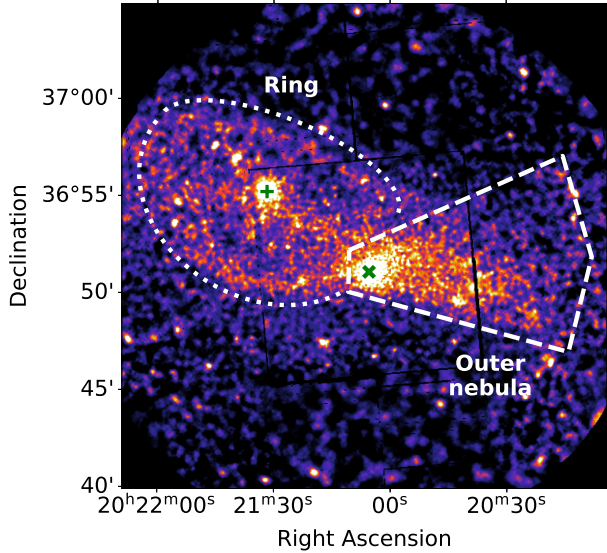


Figure 4. Merged (MOS1 and MOS2), QPB-subtracted, exposure-corrected, and smoothed XMM image in 2 – 6 keV. PSR J2021+3651 and WR 141 are marked with a cross (X) and a plus (+) sign, respectively. The extent of the outer nebula $\sim 10'$ is marked with dashed lines. A “ring” is marked with a dotted line.

masks were applied to the cleaned event files using the `mos-spectra` task to create MOS1 and MOS2 images of the entire FOV in 2 – 6 keV. The quiescent particle background (QPB) image was generated for the entire FOV in the same energy range using the `mos.back` task. Residual SP contamination was found to be negligible (see §2.3.3). No significant instrumental or SWCX background is present in the energy range of our analysis, and no significant stray light background was observed in the image. Therefore, after combining the MOS1 and MOS2 images (`comb` task), we subtracted only the QPB image, corrected the exposure, and adaptively smoothed it using the `adapt` task to create Figure 4.

Significant emissions are present on the east and west of PSR J2021+3651 (marked with X). The emission on the east of PSR J2021+3651 (“ring”-like structure, marked with dotted line) shows no low-energy counterpart in the radio (VLA L band) observation by (Roberts et al. (2008)). Mizuno et al. (2017) claimed this ring-like structure to be part of the Dragonfly. On the other hand, Van Etten et al. (2008) and Jin et al. (2023) detected a bow-shock structure from the inner nebula of the Dragonfly in the X-ray (*Chandra*) and radio (VLA C and L band) observations, respectively. Such detections indicate a supersonic motion of PSR J2021+3651 toward the east, in which case it is unlikely to expect PWN emission ahead of the bow shock formed by the pulsar. Possible origins of the emission on the west of

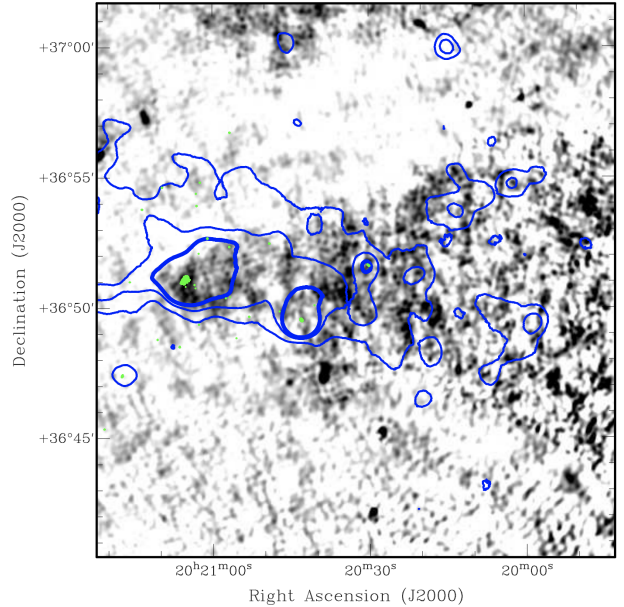


Figure 5. VLA 20cm image from Roberts et al. (2008). The radio nebula extends out to $> 20'$ from PSR J2021+3651. The XMM contours are overlaid in blue. The permission for the use of the image was acquired from AIP Publishing via RightsLink®.

the pulsar are discussed in the last paragraph of this section.

The emission on the west of PSR J2021+3651 (“outer nebula”, marked with dashed line) extends out to $\sim 10'$ with decreasing surface brightness. This X-ray nebula is spatially coincident with the first half of the radio nebula, as shown in Figure 5. The radio nebula extends further out to $> 20'$ (Roberts et al. (2008)), whose flux was used for modeling the SED of the Dragonfly (see §4). For consistency, we analyze the X-ray counterpart of the radio nebula, namely the outer nebula, and use its spectrum for SED modeling.

A ring-like structure is centered at WR 141 and has radius $\sim 5'$. The “arc” seen by *Chandra* comprises the lower part of this ring. Mizuno et al. (2017) claimed that the “ring” is part of the PWN based on the similar spectral index between the “ring” and the “outer nebula.” Barkov et al. (2019) explained the “arc” as a “kinetic jet”: pulsar wind particles that escaped into the ISM due to magnetic reconnection between the PWN and the ISM and became visible in a high $> 10 \mu\text{G}$ ISM magnetic field. A similar filamentary emission ahead of the main body of the PWN (“outer nebula”) was observed in the “Snail” PWN, whose “prongs” may be the result of the interaction between the PWN and the reverse shock of its host SNR (Temim et al. (2015)). We propose that the “ring” in our XMM image is possibly

associated with WR 141. WR stars are known to have strong stellar winds that can create a bubble of several parsecs in radius (Weaver et al. (1977)). This bubble is often observed as a ring-shaped nebula and can be visible in X-ray (e.g., Toalá et al. (2012)). The parallax of 0.5024 mas in Gaia DR3 (Collaboration et al. (2022)) implies a 2.0 kpc distance to WR 141. This yields the radius of the bubble = 2.9 pc. Part of the “ring” was also seen in H α photometry by Law et al. (2002), which the authors postulated to be part of the ring nebula photoionized by WR 141.

2.3. Spectral analysis

We present a spectral analysis of PSR J2021+3651 and its PWN using *Chandra*, XMM, and *NuSTAR* data. We first characterize the pulsar spectrum with *Chandra* taking advantage of its fine angular resolution (HPD < 0.5"). We analyze the spectrum of the inner nebula taking into account the contribution of the pulsar by individually and jointly fitting the *Chandra*, XMM, and *NuSTAR* spectra. We use the XMM data to study the spectrum of the outer nebula. All the spectral models for X-ray analysis presented in this work were multiplied by a cross-normalization factor (`const`) to adjust relative normalization between different detectors and instruments.

2.3.1. Pulsar spectrum

We used *Chandra* data to analyze the spectrum of PSR J2021+3651. We extracted the source spectra from a circular region with radius 2" centered at PSR J2021+3651, and the background spectra from an annulus around PSR J2021+3651 with radii 2 – 4" using the `specextract` command in CIAO. The source spectra were binned to have at least 3σ significance over the background in each bin. We began by fitting an absorbed power law (`const*tbabs*pow`) to the spectra in 0.5 – 7 keV where the source emission dominates over the background. The abundance table was set to `wilm` (Wilms et al. (2000)) for all the X-ray spectral analyses presented in this work. This model gives a reasonable fit ($\chi^2/d.o.f = 130/152$) with the best-fit $\Gamma = 1.73^{+0.13}_{-0.12}$ and $N_H = (0.26 \pm 0.05) \times 10^{22} \text{ cm}^{-2}$. However, this best-fit N_H is 3 times smaller than the N_H found from the *Chandra* spectra of the inner nebula. When the N_H was fixed to the best-fit value found from the *Chandra* inner nebula spectra ($0.76 \times 10^{22} \text{ cm}^{-2}$, see §2.3.2), the fit quality became worse ($\chi^2/d.o.f = 190/152$) with much softer $\Gamma = 2.87 \pm 0.15$. This is because the pulsar has significant emission in both below and above 3 keV. Initially, a small N_H was favored to explain the emission below 3 keV. Later, the Γ was significantly softened to compensate for the larger N_H , leaving the

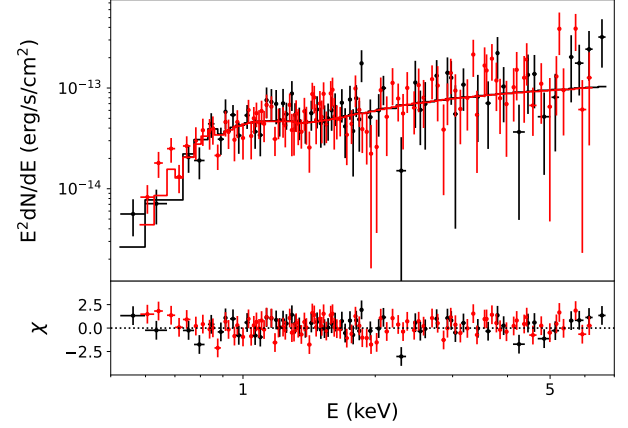


Figure 6. *Chandra* ObsID 8502 and 7603 (black and red crosses, respectively) spectra of PSR J2021+3651. The background is dominant outside of 0.5–7 keV. The source spectra were extracted from a circular region with radius 2" centered at the pulsar. The background spectra were extracted from an annulus region with radii 2 – 4" centered at the pulsar.

emission above 3 keV poorly fitted. We added a black body component to fit the emission below 3 keV while the power law component explains the emission above 3 keV (`const*tbabs*(bbod*pow)`). N_H is highly degenerate with the black body temperature and the power law index, so we fixed N_H to the *Chandra* value of the inner nebula. This gives the best-fit $kT = 0.13 \pm 0.01$ keV and $\Gamma = 1.63 \pm 0.17$ with $\chi^2/d.o.f = 123/151$. We used this model as the initial pulsar component when jointly fitting the *Chandra* spectra of the inner nebula and the XMM and *NuSTAR* spectra of the pulsar and the inner nebula (see §2.3.2). We iteratively fit the *Chandra* pulsar spectra by changing the N_H to the best-fit value found from the joint fit of the *Chandra*, XMM, and *NuSTAR* spectra. The pulsar model converged to $kT = 0.11 \pm 0.01$ keV and $\Gamma = 1.77 \pm 0.17$ with $\chi^2/d.o.f = 123/151$. The best-fit parameters are comparable to Van Etten et al. (2008) ($\Gamma = 1.73^{+1.15}_{-1.02}$, $kT = 0.16 \pm 0.02$ keV, and $N_H = 0.67 \times 10^{22} \text{ cm}^{-2}$) considering the degeneracy between kT and N_H . The unabsorbed flux of PSR J2021+3651 in 3 – 10 keV is $F_{3-10} = (1.20^{+0.18}_{-0.17}) \times 10^{-13} \text{ erg/s/cm}^2$.

2.3.2. Inner nebula spectrum

We individually and jointly fitted the *Chandra*, XMM, and *NuSTAR* spectra of the inner nebula. The *Chandra* spectra were extracted from an annulus region with radii 2 – 20" centered at PSR J2021+3651. The XMM spectra were extracted from circular regions with radius 40" using the `xmmselect` task in SAS. Response files were generated using `rmfgen` and `arfgen` tasks. *NuSTAR* spectra were extracted from circular regions

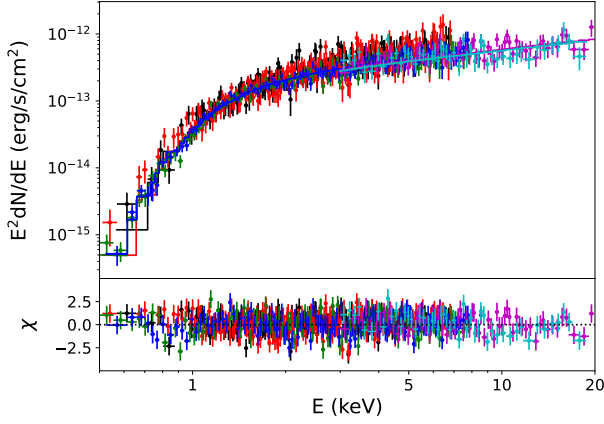


Figure 7. *Chandra* ObsID 8502 (black) and 7603 (red), XMM MOS1 (green) and MOS2 (blue), *NuSTAR* FPMA (magenta) and FPMB (cyan) spectra of the inner nebula. The background is dominant outside of 0.5–7 keV for *Chandra*, 0.5–8 keV for XMM, and 3–20 keV for *NuSTAR*. The source spectra were extracted from an annulus region with radii 2–20'' for *Chandra*, a circular region with radius 40'' for XMM, and a circular region with radius 1' for *NuSTAR*, all centered at PSR J2021+3651. The background spectra were extracted from a 2' × 2' box in a source-free region. For XMM and *NuSTAR*, the pulsar spectra were subtracted. The best-fit models are displayed as solid lines in both plots.

with radius 1' using `nuproducts` task in `NuSTARDAS`. The sizes of the source region for different instruments were determined considering the PSF sizes of the instruments ((HPD 1'' for *Chandra*, 34'' for XMM, and 58'' for *NuSTAR*) and the cross-normalization term between the source spectra. The background spectra for all three instruments were taken from a 2' × 2' box in a nearby source-free region. Fitting was performed in the energy range where the source emission dominates over the background (0.5–7 keV for *Chandra*, 0.5–8 keV for XMM, 3–20 keV for *NuSTAR*). All spectra were binned such that the source counts have at least 3σ significance above the background counts in each bin.

We first modeled the *Chandra* spectra of the inner nebula using an absorbed power law (`const*tbabs*pow`) to find the best-fit $N_H = (0.76 \pm 0.06) \times 10^{22} \text{ cm}^{-2}$. Using this N_H , the best-fit model for the pulsar was found ($kT = 0.13 \pm 0.01 \text{ keV}$, $\Gamma = 1.63 \pm 0.17$, see §2.3.1). This pulsar component was included and held fixed in the model for the XMM and *NuSTAR* spectra of the inner nebula. The N_H for both instruments were held fixed to the value found from the *Chandra*-only fit. The best-fit Γ for *Chandra* and XMM are in good agreement (1.25 ± 0.06 and 1.35 ± 0.03 , respectively), while the *NuSTAR* spectra give much softer $\Gamma = 1.73 \pm 0.07$. We jointly fitted the *Chandra*, XMM, and *NuSTAR* spectra

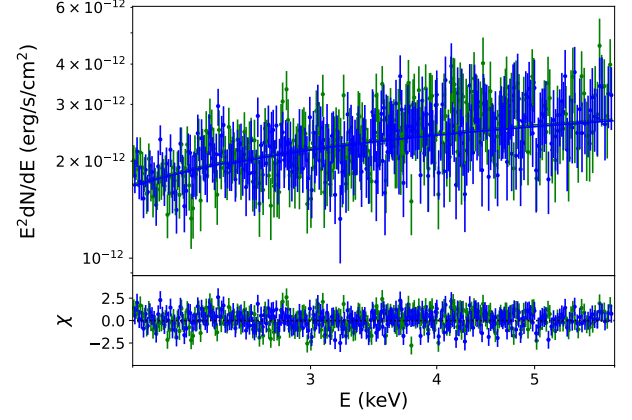


Figure 8. XMM MOS1 and MOS2 (green and blue, respectively) spectra of the outer nebula. The source spectra were extracted from the dashed polygon in Figure 4. The line and continuum backgrounds are dominant below 2 keV and above 6 keV, respectively. The best-fit models are displayed as solid lines.

to constrain the model for the inner nebula more tightly and to test the presence of a spectral break. The iterative fitting of the pulsar spectrum was performed in parallel (see §2.3.1). An absorbed power law model with $N_H = (0.96 \pm 0.04) \times 10^{22} \text{ cm}^{-2}$ and $\Gamma = 1.49 \pm 0.03$ explains the spectra well ($\chi^2/d.o.f = 710/705$). Adding a break to the power law does improve the fit (F test probability = 0.002); however, the break energy $E_{\text{break}} = 6.02^{+0.75}_{-1.19} \text{ keV}$ near the borderline between the *Chandra* and XMM vs. *NuSTAR* energy ranges is suspect. We concluded that the hint of spectral break might originate from the imperfect cross-calibration between the different instruments. The unabsorbed flux of the inner nebula is $F_{3-10} = (5.31 \pm 0.21) \times 10^{-13} \text{ erg/s/cm}^2$. The best-fit Γ for the inner nebula from the joint fit is comparable with Van Etten et al. (2008) (1.45 ± 0.09).

2.3.3. Outer nebula spectrum

We used the XMM data to analyze the outer nebula spectrum. The cleaned event files and the Swiss cheese masks (see §2.2.3) were processed with the `mos-spectra` task to extract the source spectra from the dashed polygon in Figure 4. We followed the procedures described in the manual for the use of `XMM-ESAS`¹ to carefully estimate the background in such a large source region ($\sim 10'$). First, the QPB spectra were generated for the same region using the `mos_back` task. Second, the background spectrum below 2 keV contains multiple instrumental and solar wind charge exchange (SWCX) lines.

¹ <https://heasarc.gsfc.nasa.gov/FTP/xmm/software/xmm-esas/xmm-esas-v13.pdf>

Table 1. Summary of X-ray spectral analysis results

Region	Instrument [†]	Energy (keV)	N_H (10^{22} cm^{-2})	kT (keV)	Γ	F_{3-10} ($10^{-13} \text{ erg/s/cm}^2$)	$\chi^2/d.o.f$
Pulsar	C	0.5 – 7	0.96 [‡]	0.11 ± 0.01	1.77 ± 0.17	$1.20^{+0.18}_{-0.17}$	128/151
	C	0.5 – 7	0.76 ± 0.06	–	1.26 ± 0.06	$6.80^{+0.32}_{-0.31}$	345/349
Inner	X	0.5 – 8	0.76 [‡]	–	1.35 ± 0.03	$5.58^{+0.18}_{-0.17}$	246/240
nebula	N	3 – 20	0.76 [‡]	–	1.73 ± 0.07	5.50 ± 0.22	106/114
	C+X+N	0.5 – 20	0.96 ± 0.04	–	1.49 ± 0.03	5.31 ± 0.21	710/705
Outer nebula	X	2 – 6	0.96 [‡]	–	1.82 ± 0.03	32.53 ± 0.69	509/541

[†] C = *Chandra*, X = XMM, N = *NuSTAR*. [‡] held fixed.

We chose 2 – 6 keV for the energy range of our analysis to avoid modeling too many background components. The continuum background dominates over 6 keV. Third, we attempted to model the remaining background components on **Xspec**: SP residuals and the cosmic X-ray background (CXB). The QPB spectra were loaded as background spectra. The source spectra were binned to have at least 3σ significance over the QPB spectra in each bin. The background from SP residuals was modeled with a power law using unitary response matrices, but none of the model parameters were constrained. Therefore we assumed that the contribution from residual SP is insignificant and excluded it from the model. The CXB was modeled with an absorbed power law (**const*tbabs*pow**). All of its model parameters were fixed to the canonical values ($\Gamma = 1.41$, normalization=11.6 photons/keV/s/cm²/sr at 1 keV, De Luca, A. & Molendi, S. (2004)) to circumvent the degeneracy between the two power-law components (CXB and the outer nebula). We used the Galactic hydrogen column density² at the center of the source extraction region (1.13 cm^{-2}) as the N_H for the CXB.

The outer nebula was modeled with an absorbed power law (**const*tbabs*pow**). The N_H is not constrained in the energy range of this analysis (2 – 6 keV). We fixed the N_H to the best-fit value found from the *Chandra*, XMM, and *NuSTAR* joint fit of the inner nebula ($0.96 \times 10^{22} \text{ cm}^{-2}$). The best-fit model with $\Gamma = 1.82 \pm 0.03$ yields a reasonable fit ($\chi^2/d.o.f = 509/541$). The unabsorbed flux of the outer nebula in 2 – 10 keV is $F_{2-10} = (4.20 \pm 0.07) \times 10^{-12} \text{ erg/s/cm}^2$. The best-fit Γ is clearly harder than Mizuno et al. (2017) ($\Gamma = 2.10 \pm 0.12$), yet the flux value is comparable ($F_{2-10} \sim 4.1 \times 10^{-12} \text{ erg/s/cm}^2$ for the PWN-west).

3. FERMI ANALYSIS

The gamma-ray pulsations of PSR J2021+3651 was first detected by AGILE (Halpern et al. (2008)) and later

confirmed by *Fermi* (Abdo et al. (2009)). The pulsar is registered in the most recent *Fermi*-LAT source catalog (4FGL-DR3, *Fermi-LAT collaboration et al. (2022)*) as 4FGL J2021.1+3651. We analyzed 13-year *Fermi* data (August 2008 – October 2021, MET 239557417 – 656813666) to detect the GeV emission from the Dragonfly. We selected SOURCE class and FRONT+BACK type events (evclass=128, evtype=3) and used the instrument response functions (IRFs) **P8R3_SOURCE.V3**. The 90° zenith angle cut and the filter expression **DATA_QUAL>0 && LAT_CONFIG==1** were applied. The region of interest (ROI) is a $10^\circ \times 10^\circ$ box region centered at 4FGL J2021.1+3651.

We performed a binned likelihood analysis (spatial bin = 0.1° , energy bin = 8 bins per decade) using **Fermipy v1.0.1** (Wood et al. (2017)). The ROI model includes the 4FGL-DR2 sources (**gll_psc_v27.fit**, Ballet et al. (2020)) within a 30×30 box region centered on 4FGL J2021.1+3651, the Galactic diffuse emission model (**gll_iem_v07.fits**), and the isotropic emission model (**iso_P8R3_SOURCE.V3_v1.txt**)³. We used the **optimize()** and **fit()** methods in **Fermipy** to optimize the model in 100 MeV – 300 GeV. For the **fit()** method, the parameters of bright nearby sources (within 5° of 4FGL J2021.1+3651 and TS (test statistics) > 25) were left free. After fitting, the residual map was visually inspected, and a standard normal distribution was fitted to the residual significance histogram to ensure that the residuals are statistical fluctuations.

4FGL J2021.1+3651 is modeled with **PLSuperExp-Cutoff2**⁴. The best-fit parameters of 4FGL J2021.1+3651 agreed with those of 4FGL-DR2 within 1σ error. Since the emission from 4FGL J2021.1+3651 cuts off in the 10–30 GeV range, we created a $\sqrt{\text{TS}}$ map of the ROI above 30 GeV to avoid contamination

³ <https://fermi.gsfc.nasa.gov/ssc/data/access/lat/BackgroundModels.html>

⁴ https://fermi.gsfc.nasa.gov/ssc/data/analysis/scitools/source_models.html

² <https://www.swift.ac.uk/analysis/nhtot/>

by the pulsar and investigate any possible diffuse emission from the PWN. We did not find any excess in the vicinity of 4FGL J2021.1+3651 that can be attributed to the emission from the PWN. This result confirms the non-detection of the GeV PWN in the vicinity of PSR J2021+3651 from the previous studies of the off-pulse data (Abdo et al. (2009)).

GeV gamma rays are IC upscattered photons off the low energy electrons that emit synchrotron radiation in radio – infrared. Given the large ($> 20'$) size of the radio nebula, a putative GeV nebula may be largely extended and too faint to be significantly detected over the background. The large ($\sim 1^\circ$) size of the IC nebula in the VHE range (eHWC J2019+368) may also indicate a largely extended GeV nebula. Acero et al. (2013) calculated upper limits for a GeV PWN of PSR J2021+3651 assuming a size of MGRO J2019+37. Di Mauro et al. (2021) used an ICS template with the best-fit diffusion coefficient for eHWC J2019+368 to place GeV upper limits of the PWN. Both works resulted in GeV upper limits similar to the flux of eHWC J2019+368.

4. MW SED MODELING

Figure 9 shows the MW counterparts of the Dragonfly overlaid on the HAWC significance map. PSR J2021+3651 is located at the Eastern edge of the extended TeV source eHWC J2019+368. Its PWN, the Dragonfly, extends toward the centroid of eHWC J2019+368. We model the SED of the Dragonfly using these MW data to investigate the Dragonfly as a leptonic PeVatron.

While our *NuSTAR* observation allowed an in-depth study of the inner nebula, the faint emission from the outer nebula was not detected due to the limited sensitivity. Instead, we used our XMM analysis result of the outer nebula presented in §2.3.3. The radio spectrum and the GeV upper limits were taken from Roberts et al. (2008) and Di Mauro et al. (2021) (“IEM-4FGL”), respectively. In the TeV band, three independent flux measurements by VERITAS (VER J2019+368), HAWC (eHWC J2019+368), and LHAASO (LHAASO J2018+3651) are available. Cao et al. (2021a) did not provide detailed spectral information of LHAASO J2018+3651 except for its flux at 100 TeV. Abeysekara et al. (2018) and Abeysekara et al. (2020) provide the spectrum of VER J2019+368 and eHWC J2019+368, respectively, over three decades of energy. While VER J2019+368 and eHWC J2019+368 exhibit similar source size, the flux of VER J2019+368 reported in Abeysekara et al. (2018) was extracted from a region smaller than the source size, yielding a 2–3 times lower flux than that of eHWC J2019+368 in the overlapping energy range

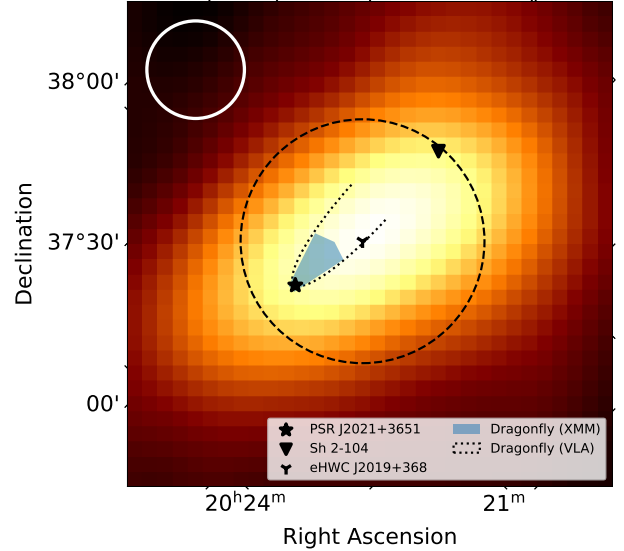


Figure 9. HAWC significance map ($2^\circ \times 2^\circ$) centered at the centroid of eHWC J2019+368. The eHWC J2019+368 flux extraction region is marked with a dashed circle (radius 0.5°). PSR J2021+3651 and Sh 2-104 are marked with a star and a triangle, respectively. The shaded region is the XMM spectrum extraction region of the outer nebula. The dotted line shows the extent of the outer nebula seen by VLA. The angular resolution of HAWC varies depending on the energy and zenith angle. The approximate size of the 68% containment region at 56 TeV (radius 0.2°) is marked with a solid white circle at the top left corner.

The HAWC image was obtained from the 3HWC survey public data (<https://data.hawc-observatory.org/datasets/3hwc-survey/fitsmaps.php>), and the VLA nebular extent was estimated from Roberts et al. (2008).

(see also Albert et al. (2021)). Therefore, we used the spectrum of eHWC J2019+368 from Abeysekara et al. (2020) for SED modeling in this work.

The distance estimates of PSR J2021+3651 vary widely depending on different distance measures. Roberts et al. (2002) used the dispersion measure (DM) $\sim 371 \text{ pc cm}^{-3}$ to put the pulsar at $\geq 10 \text{ kpc}$ on the outer edge of the Galaxy, although they left a possibility of a nearer distance in case of a contribution from excess gas in the Cygnus region. Van Etten et al. (2008) suggested 3–4 kpc based on various arguments, such as the X-ray spectral fit to a neutron star atmosphere model and the gamma-ray efficiency of the pulsar. Abdo et al. (2009) estimated a distance $\geq 4 \text{ kpc}$ based on the pulsar rotation measure (RM). Kirichenko et al. (2015) suggested $1.8^{+1.7}_{-1.4} \text{ kpc}$ using the interstellar extinction and distance relation. The 1.8 kpc distance was adopted by Mizuno et al. (2017), Fang et al. (2020), and Albert et al. (2021) for their MW SED modeling.

Table 2. Best-fit SED model parameters using Naima

α	2.4
E_{cut}	0.9 PeV
Magnetic field	1.6 μ G
IR temperature	26 K
IR energy density	1.0 eV/cm ³
Total particle energy [†]	$6.1d_{3.5}^2 \times 10^{49}$ erg

[†] $d_{3.5}$ is the distance to the Dragonfly scaled to the nominal distance of 3.5 kpc.

We start with preliminary modeling of the MW SED using *Naima* (Zabalza (2015)), a generic model for non-thermal radiation from relativistic particles. We do not make assumptions about the distance or evolutionary history of the PWN at this stage. Our purpose for this preliminary modeling is to provide a basic understanding of the current status of the PWN and initial estimation of the input parameters for a more sophisticated model, namely the dynamical model (Gelfand et al. (2009)). Then we move on to MW SED modeling using the dynamical model to acquire insight into the dynamical evolution of the Dragonfly over its lifetime while the interactions between the PWN, SNR, and ISM are accounted for.

4.1. *Naima*

Naima allows us to characterize the current particle population using a minimal number of parameters without introducing any physical assumptions on the evolutionary history of the system.

For a leptonic particle accelerator, synchrotron (SC) emission and emission via inverse Compton (IC) scattering off the input seed photon fields (cosmic microwave background (CMB) and interstellar dust emission (infrared, or IR)) are calculated based on a particle distribution model. We vary the model parameters of a single particle distribution so that the SC and IC spectra are consistent with the observed flux in radio, X-ray, and TeV gamma-ray bands. The minimum particle energy (E_{min}) and the reference energy (E_0) were fixed to 1 MeV and 1 TeV, respectively. The best-fit parameters are summarized in Table 2, and the best-fit SED model is plotted with the MW data and residuals in Figure 10.

The TeV spectrum exhibits a smooth cutoff after 20 TeV. This cutoff is better explained by an exponential cutoff power law distribution of particles, $dN/dE = A(E/E_0)^{-\alpha}e^{-E/E_{cut}}$, than a simple power law with a sharp cutoff at E_{max} . The best-fit particle index is $\alpha = 2.4$. Adding an IR field gives a better fit than the CMB-only model, although the IR field energy density tends to grow indefinitely to an unphysical value. There-

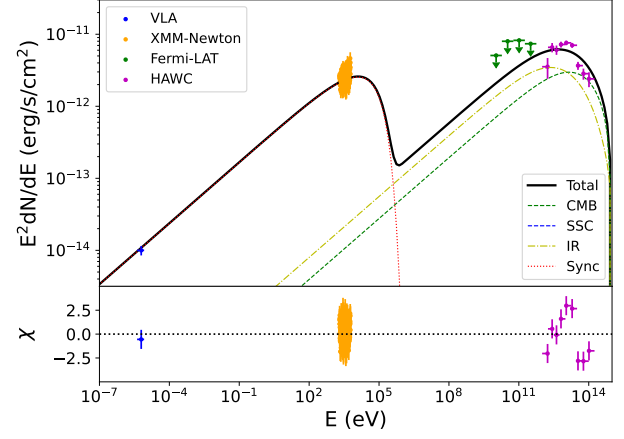


Figure 10. The best-fit SED model from *Naima*. The model parameters are given in Table 2. Synchrotron flux (Sync), inverse Compton flux from the CMB (CMB), infrared emission from the interstellar dust grains (IR), synchrotron self-Compton component (SSC), and total flux are plotted. The SSC flux level is very low and located below the lower bound of the y-axis. Radio, X-ray, and TeV flux data points, and GeV upper limits are overlaid. The residuals are plotted in terms of significance $((\text{data} - \text{model}) / (1\sigma \text{ uncertainty of data}))$.

fore we fixed the IR field energy density to the average cosmic ray energy density (1 eV/cm³, Cummings et al. (2016)). This yields the best-fit IR field temperature $T = 26$ K, magnetic field $B = 1.6 \mu$ G, and cutoff energy $E_{cut} = 0.9$ PeV. This SED model shows a good fit to the MW data as seen in the residuals plotted in Figure 10; however, the narrow IC peak resolved by HAWC is difficult to explain with physically reasonable model parameters. Such a narrow peak originates from the flux point in the lowest energy bin, the range in which air imaging Cherenkov telescopes (IACTs), such as VERITAS, are more sensitive. A deeper VERITAS observation and more accurate flux measurement of the region have been proposed for our future work to resolve the IC spectrum of the Dragonfly better.

The best-fit cutoff energy $E_{cut} = 0.9$ PeV strongly suggests that the Dragonfly is likely a PeVatron. The cutoff energy is greater than 0.3 PeV by Albert et al. (2021) and 0.4 PeV by Fang et al. (2020) mainly due to the difference in the X-ray spectra used in each work (see §4). The magnetic field inside the PWN is at the level of interstellar magnetic field ($\sim 3 \mu$ G, Jansson & Farrar (2012)), as one may infer from the low X-ray to gamma-ray luminosity ratio.

The IR field temperature is higher than the IR emission from cold dust grains (~ 15 K). A possible source of this warm dust emission is an H II region Sh2-104 (marked with an inverted triangle in Figure 9). Lo-

cated at 4 ± 0.5 kpc from the Earth, Sh2-104 is visible in radio through X-ray (Deharveng, L. et al. (2003), Rodón et al. (2010), Xu et al. (2017), and Gotthelf et al. (2016)). Sh 2-104 hosts an ultra-compact H II (UCHII) region on the eastern periphery of its dense molecular shell. As strong candidates for active star formation (Deharveng, L. et al. (2003) and Xu et al. (2017)), Sh2-104 and the UCHII region each contain a stellar cluster, MASS J20174184+3645264 and IRAS 20160+3636, respectively, ionizing the regions (Deharveng, L. et al. (2003) and Paredes et al. (2009)). Rodón et al. (2010) used Herschel observations to estimate the dust temperature in Sh2-104 to be 20 – 30 K on the exterior. Our best-fit IR field temperature (26 K) lies in this temperature range. Since the lower bound of the distance to Sh2-104 (Deharveng, L. et al. (2003)) and the upper bound of the distance to PSR J2021+3651 Kirichenko et al. (2015) coincide (3.5 kpc), we adopt 3.5 kpc as a nominal distance to the Dragonfly hereafter and scale relevant parameters to this distance whenever possible.

4.2. Dynamical model

Taking the result from *Naima* as a starting point, we fit the dynamical model to the MW data of the Dragonfly. The dynamical model is a time-evolutionary model for a composite system of a PWN and its host SNR. The model assumes a spherical single-zone system whose SNR is in a free-expansion or Sedov-Taylor phase. The model evolves a PWN and its SNR from their birth to the true age of the system, calculating the interaction between them and with the surrounding interstellar medium (ISM). The model output includes a pulsar wind particle distribution, its synchrotron and inverse Compton emission spectrum, and the dynamics of a system (e.g., a radius of a PWN, a radius of an SNR forward and reverse shock, and a magnetic field inside a PWN) at each evolutionary phase.

The dynamical model evolves the particle distribution inside a PWN via three mechanisms: continuous particle injection of a fraction of the pulsar spin-down luminosity, adiabatic energy loss due to the expansion of the PWN, and radiative energy loss due to synchrotron and inverse Compton emission. The spin-down luminosity \dot{E} of a PWN at its age t is formulated as

$$\dot{E}(t) = \dot{E}_0 \left(1 + \frac{t}{\tau_{sd}} \right)^{-\frac{p+1}{p-1}}, \quad (1)$$

where \dot{E}_0 is the initial spin-down luminosity, p is the pulsar braking index, and τ_{sd} is the characteristic pulsar spin-down timescale. τ_{sd} is related to a pulsar's characteristic age τ and true age t_{age} as

$$t_{age} = \frac{2\tau}{p-1} - \tau_{sd}. \quad (2)$$

Table 3. SED model parameters using the dynamical model

Source distance		3.5 kpc
Input	E_{SN}	1.0×10^{51} erg
	M_{ej}	$7.2 M_{\odot}$
	n_{ISM}	0.03 cm^{-3}
	Braking index p	2.5
	Age	16 kyr
	η_B	0.008
	E_{max}	1.4 PeV
	Particle index α	2.4
	IR field temperature	9.9 K
	IR field energy density	1.4 eV cm^{-3}
Output	t_{RS}	12 kyr
	R_{PWN}	9.5 pc
	Magnetic field	$2.7 \mu\text{G}$
	Total particle energy	3.9×10^{48} erg

A fraction of the spin-down luminosity $\eta_B \dot{E}$ is injected into the PWN as magnetic fields, while the rest of the spin-down luminosity, $(1 - \eta_B) \dot{E}$, is injected as particles (electrons and positrons). The particle injection spectrum is defined within the energy range between E_{min} (minimum energy of the injected particle, fixed to 0.1 GeV in this work) and E_{max} (maximum energy of the injected particle). The magnetic field is assumed to be homogeneous throughout the volume of the PWN, and thus it decreases as the PWN expands and increases as the PWN is crushed by the collision with the SNR reverse shock. The radiative loss changes accordingly – synchrotron emission is much stronger than inverse Compton emission in the early stage or post-collision era of the PWN, whereas inverse Compton flux becomes comparable with synchrotron flux as the PWN ages. Adiabatic loss is most severe when a PWN freely expands against only ram pressure from the unshocked SN ejecta in the free-expansion phase. Once the PWN collides with the SNR reverse shock and starts encountering the pressure from shocked ejecta, the expansion of the PWN slows down until the compression starts, during which the PWN undergoes adiabatic heating.

The dynamical evolution of a system is calculated based on input parameters related to a supernova (SN), SNR, and surroundings, such as SN explosion energy (E_{SN}), ejecta mass inside an SNR (M_{ej}), and ISM density just outside an SNR forward shock (n_{ISM}). These parameters determine the pressure just outside a PWN and at the location of a reverse shock. A PWN size changes such that the pressure from the ejecta is in balance with the pressure inside a PWN, which comprises magnetic pressure and pressure from particles as a relativistic ideal gas. When a reverse shock reaches a PWN,

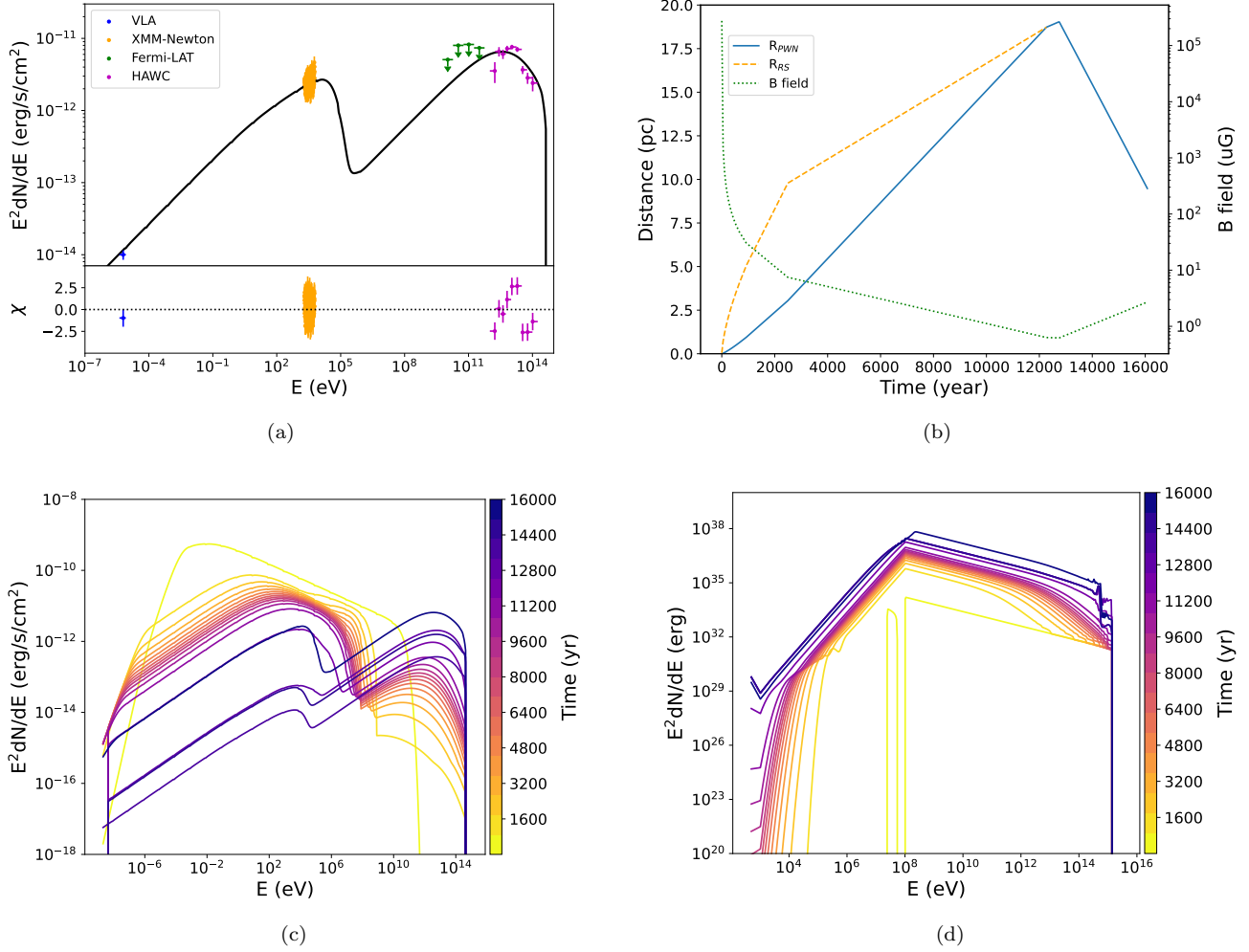


Figure 11. (a) The SED model for the Dragonfly from the dynamical model. The model parameters are given in Table 3. Radio, X-ray, and TeV flux data points are overlaid. The residuals are plotted in terms of significance ($(\text{data} - \text{model}) / (1\sigma \text{ uncertainty of data})$). (b) Time evolution of the PWN radius (R_{PWN} , blue solid line), SNR reverse shock radius (R_{RS} , orange dashed line), and magnetic field inside the PWN (B field, green dotted line) over the true age from our model (16 kyr). The PWN collided with the SNR reverse shock at $t_{RS} = 12$ kyr. (c)(d) Time evolution of the radiation (c) and particle (d) spectrum of the Dragonfly.

the pressure experienced by a PWN increases dramatically. This leads to a rapid decrease in the size of a PWN and, consequently, a sharp increase in the magnetic field inside a PWN. Synchrotron loss is extreme at this point. Once a PWN is highly compressed, and its pressure exceeds the ejecta pressure, the PWN starts re-expanding, and hence the magnetic field inside the PWN starts decreasing. As a PWN ages, its size grows as large as several parsecs or more, and its magnetic field becomes as low as a few μ G. The resulting spectrum yields a similar level of SC and IC flux, a typical spectrum observed in middle-aged PWNe.

We aimed to find a set of model parameters that reproduces not only the MW spectrum but also the observed size of the Dragonfly. The Dragonfly displays a

highly asymmetric morphology, although the dynamical model assumes a spherical system. Given this limitation of the model, we focus on characterizing the evolution of the PWN properties averaged over the entire system rather than their spatial dependency. We approximated a nominal radius of the PWN to be $10'$ so that its spherical volume roughly matches the physical volume of the outer nebula. The radio nebula size $\sim 20'$ was used for this calculation – the lowest energy particles seen in the radio band would have a much longer lifetime than its synchrotron cooling time and thus best reflect the true extent of the PWN. The angular size of $10'$ is equivalent to $R_{PWN} = 10$ pc at the nominal distance $d = 3.5$ kpc.

The input and output parameters of the dynamical model are listed in Table 3. Figure 11 shows the SED

Table 4. Comparison between PeVatron pulsar wind nebulae

		G75.23+0.12 (“Dragonfly”)	G18.5-0.4 (“Eel”) ^a	G106.65+2.96 (“Boomerang”) ^b
TeV counterpart		eHWC J2019+368 LHAASO J2018+3651	HAWC J1826-128 LHAASO J1825-1326	HAWC J2227+610 LHAASO J2226+6057
Name		PSR J2021+3651	PSR J1825-1256	PSR J2220+6114
Pulsar	τ (kyr)	17	14	10
	\dot{E} (10^{36} erg/s)	3.4	3.6	22
	Distance ^c (kpc)	0.4 – 12 (3.5)	3.5	0.8 – 7.5 (7.5)
	E_{max} (PeV)	1.4	4.6	3.3
PWN	Magnetic field (μ G)	2.7	0.6	2.2
	True age (kyr)	16	4.6	3.3
	t_{RS} (kyr)	12	–	1.5

^aBurgess et al. (2022) and references therein. ^bPope et al. (submitted to ApJ) and references therein.

^cFor the sources with a wide range of distance estimates, the distance used for SED modeling is given in parentheses.

model plotted with the MW data and residuals, the time evolution of the dynamical parameters (magnetic field, PWN radius R_{PWN} , and SNR reverse shock radius R_{RS}), radiation and particle spectra.

The maximum particle energy $E_{max} = 1.4$ PeV provides strong evidence that the Dragonfly is a PeVatron PWN. The true age of 16 kyr was found to be slightly younger than its characteristic age $\tau = 17$ kyr. The true age found by our model is much older than 7 kyr found by Albert et al. (2021). This difference can be attributed most likely to the assumed source distance (3.5 kpc in this work, 1.8 kpc in Albert et al. (2021)), as well as to the SED models and the X-ray spectra (see §4). The low magnetic field (2.7 μ G) is consistent with that from Naima, Mizuno et al. (2017), Fang et al. (2020), and Albert et al. (2021). The low magnetic fraction $\eta_B = 0.008$ contributes to this low magnetic field.

Our model predicts that the PWN expanded to ~ 20 pc, collided with the SN reverse shock 4 kyrs ago ($t_{RS} = 12$ kyr), and has been shrinking since then to reach the current size ~ 10 pc (Figure 11 (b)). Relatively low ISM density $n_{ISM} = 0.03$ cm⁻³ drove a slow reverse shock, allowing the PWN to grow large enough to reach the reverse shock even before it started heading back toward the PWN. Combined with the substantial ejecta mass $M_{ej} = 7.2M_{\odot}$, this low ISM density may indicate that the host SNR of the Dragonfly evolved into the wind-blown bubble of a massive progenitor star with an extremely low density (below 0.001 cm⁻³) during the first few kyrs of its lifetime (Dwarkadas (2005)).

The particle index $\alpha = 2.4$ is consistent with Naima. The IR field temperature (9.9 K) falls below the range of the dust temperature in Sh2-104 (see §4.1). Using the braking index $p = 2.5$ and $\tau_{sd} = 6.8$ kyr of our model, the total particle energy (3.9×10^{48} erg) is 50% of the

total injected energy over the true age (16 kyr) of the Dragonfly.

5. DISCUSSION

5.1. PeVatron pulsar wind nebulae

We compare three PeVatron PWNe studied in our *NuSTAR* observational program of energetic PWNe: G75.23+0.12 (“Dragonfly”, this work), G18.5-0.4 (“Eel”, Burgess et al. (2022)), and G106.65+2.96 (“Boomerang”, submitted to ApJ). All three PWNe were modeled with the dynamical model. Key facts and the model parameters of the three PWNe are summarized in Table 4. The common features of the three PeVatron PWNe are the following:

1. The maximum particle energy is greater than 1 PeV.
2. The source morphology is highly asymmetric and energy-dependent. The pulsar is located on the edge of the extended radio and soft X-ray nebulae and is offset from the centroid of its TeV counterparts.
3. The magnetic field strength inside the PWNe is low < 3 μ G.
4. Compact hard X-ray nebula was detected up to 20 keV by *NuSTAR*. The nebular size is much smaller than the lower-energy nebula (radio and soft X-ray).
5. The compact hard-Xray nebular spectrum does not exhibit a spectral break or cutoff. A synchrotron burnoff is observed from the shrinkage of its size at higher energies.
6. The dynamical model predicts that the PWN collided with the reverse shock of the host SNR “re-

cently” (the Dragonfly and Boomerang), or such a collision is about to happen (the Eel).

2 and 3 are known properties of bright TeV PWNe (e.g., Kargaltsev et al. (2013) and Torres (2017)). While asymmetric morphology bears a few different possibilities (fast pulsar velocity, asymmetric SNR reverse shock – PWN interaction, or a combination of both effects – see §5.2), energy dependency of morphology can be attributed to particle transport and cooling. Particles that emit synchrotron radiation in the radio band (particle energy $E_\gamma \sim 1$ GeV in the interstellar magnetic field $\sim 3 \mu\text{G}$) have cooling times much longer than the age of the PWN and hence transport to large distances away from the pulsar without losing much of their energies. Particles that radiate in the hard X-ray band ($E_\gamma \sim 100$ TeV), on the other hand, have much shorter cooling times than the PWN age. Such particles can travel only to short distances before cooling down to lower energies, resulting in 4 (see §5.3). Therefore, only freshly injected highly energetic particles contribute to the compact hard X-ray nebula. Relic particles, after cooling, exhibit larger extents in lower energies.

Looking at an IC spectrum, relic particles with energies $E_\gamma \sim 10$ TeV upscatter the CMB photons to TeV energies. Such particles can be dim in the synchrotron spectrum due to a lower magnetic field farther away from the pulsar, explaining the offset of the TeV emission from the pulsar. 3 is necessary for this reason and manifests as the observed low X-ray to gamma-ray luminosity ratios. GeV-emitting particles ($E_\gamma \sim 10$ GeV) are expected to form even fainter SC and IC nebulae due to their lower energies and larger distances traveled. No GeV nebulae were detected for the PeVatron PWNe except for the “tail” region of the Boomerang whose emission is attributed to its parent SNR (e.g., Fang et al. (2022)).

6 provides a hint as to how particles are accelerated in PeVatron PWNe. Ohira et al. (2018) proposed using a Monte Carlo simulation that particles may be accelerated to 1 PeV during the compression of a PWN by the collision with the reverse shock of its host SNR.

Some of the above properties are in contrast to those of other TeV PWNe in our *NuSTAR* observational campaign, such as G313.54+0.23 (“K3” or “Kookaburra”, Park et al. (2023b)) and G313.3+0.1 (“Rabbit”, Park et al. (2023a)). These southern sources are invisible to HAWC and LHAASO, the telescopes that operate in the highest energy regime (> 100 TeV). Their *NuSTAR* hard X-ray nebulae are extended (radius $\sim 3'$ at the source distance ~ 5.6 kpc for both PWNe), and the nebular sizes do not change significantly with energy. Multi-zone SED modeling using the spatially resolved

NuSTAR spectra along with MW flux data yielded the maximum particle energies below 1 PeV for both PWNe. The PWNe have bright GeV counterparts whose spectra connect smoothly to the spectra of their TeV counterparts. Future gamma-ray observatories in the southern hemisphere, the Southern Wide-field Gamma-ray Observatory (SWGO) and Cherenkov Telescope Observatory (CTAO) – South, will play a crucial role in studying the true energetics of these PWNe and their relation to the MW observations.

5.2. Distance and proper motion

The distance of the Dragonfly is relevant to not only its brightness but also its physical size, and hence the proper motion of PSR J2021+3651. Like many other TeV PWNe (e.g., H.E.S.S. Collaboration et al. (2018)), the Dragonfly is offset from the center of the nebula and its TeV counterparts. Such highly asymmetric morphology is often attributed to a fast proper motion of the pulsar. Aliu et al. (2014) estimated the transverse velocity of PSR J2021+3651 to be $840d_5t_{17}^{-1}$ km/s, where d_5 is the distance of the Dragonfly scaled to 5 kpc and t_{17} is the age of PSR J2021+3651 scaled to its characteristic age of 17 kyr, in case it was born at the end of the radio nebula. Albert et al. (2021) estimated it to be $\sim 1,300$ km/s in case PSR J2021+3651 is located at 1.8 kpc and was born 7 kyrs ago at the location of HAWC J2019+368. Van Etten et al. (2008) and Jin et al. (2023) claimed the detection of a bow shock structure on the East side of the Dragonfly, yet noted a possibility of at most a mildly supersonic motion of PSR J2021+3651 considering the well-preserved substructures of the inner nebula.

Given the true age of 16 kyr from our model, the Dragonfly may be too young to have escaped its host SNR and form a bow shock in the ISM (e.g., Gaensler & Slane (2006)). Instead, the bow shock structure with the well-defined inner nebula and the asymmetric PWN morphology could be explained by an asymmetric interaction between the PWN and the reverse shock of its host SNR due to an ambient density gradient (e.g., Temim et al. (2015) and Temim et al. (2017)). In this case, the orientation of the bow shock does not necessarily align with the direction of the pulsar’s proper motion (Kolb et al. (2017)). There is no known dense object on the East of PSR J2021+3651, and the host SNR has not been detected. This mystery could be solved by a deep and expansive radio observation that covers a large ($\sim 1^\circ$) region to search for the faint host SNR of PSR J2021+3651. Here, we focus on discussing the proper motion of PSR J2021+3651 that may have caused the asymmetric morphology of the Dragonfly.

The angular separation between PSR J2021+3651 and the centroid of eHWC J2019+368 is $\sim 16'$. If PSR J2021+3651 was born near the centroid of eHWC J2019+368 and traveled to the current location at a constant speed, the corresponding transverse velocity of the pulsar is $v_{psr} = 996d_{3.5}t_{16}^{-1}$ km/s, where t_{16} is the true age scaled to 16 kyr. This is above the average pulsar velocity (540 km/s, Verbunt et al. (2017)), but not exceptionally high (Kargaltsev et al. (2017)). In this case, measuring the pulsar proper motion of $\sim 0.06''d_{3.5}t_{16}^{-1}$ /yr may not be feasible unless PSR J2021+3651 is significantly closer than 3.5 kpc or significantly younger than 16 kyr. Another *Chandra* observation of PSR J2021+3651, nearly 20 years after the last observation, to detect the pulsar motion could provide insight into the source distance and age; however, their degeneracy will still need to be disentangled. Our future work will combine new radio (VLA) and X-ray (*Chandra*) observation with an energy-dependent morphology study using VERITAS and *Fermi*-LAT to place tight constraints on the source distance and evolutionary history of the Dragonfly.

5.3. Magnetic field

For particles with a synchrotron lifetime shorter than the age of the system, the distance that a particle can travel is determined by its synchrotron lifetime rather than the system age. In the vicinity of the pulsar where the magnetic field is strong, and the particles are transported mainly by energy-independent advection, the PWN size in different energy bands should be proportional to the synchrotron lifetime of the electrons (e.g., Tang & Chevalier (2012)). This is demonstrated by the changing nebula size in energy observed with *NuSTAR*. A synchrotron lifetime t_{sync} can be defined as a time scale that an electron with Lorentz factor γ loses all of its energy E_γ via synchrotron radiation in magnetic field strength B . A synchrotron spectrum of a single electron is highly peaked around its critical frequency $\nu_{crit}(\gamma) \propto BE_\gamma^2$. A rough estimation of a synchrotron lifetime using this information yields

$$t_{sync} = \frac{E_\gamma}{P_{synch}} \sim \frac{\gamma mc^2}{\gamma^2 B^2} \sim \frac{1}{\sqrt{B^3 \nu_{crit}(\gamma)}}. \quad (3)$$

Assuming a constant average magnetic field and advection velocity in the region, the ratio of a synchrotron lifetime between particles emitting 3 keV photons and those emitting 6 keV photons is calculated as $\sqrt{6 \text{ keV}/3 \text{ keV}} = 1.4$. This ratio is indeed comparable to the ratio of the nebula size in two different energy bands: $\text{FWHM}(3\text{--}6 \text{ keV})/\text{FWHM}(6\text{--}20 \text{ keV}) = 26.5''/15.2'' = 1.3$.

Comparing the nebula sizes in the two energy bands also allows placing an upper limit of the magnetic field inside the compact nebula. The inner nebula detected by *NuSTAR* is located well outside the termination shock (2–3 smaller than the torii $\sim 10''$ (Van Etten et al. (2008))), where the advection velocity can be approximated to the overall PWN expansion velocity (e.g., Porth et al. (2016)). The expansion velocity of the Dragonfly has not been measured, yet some other PWNe were estimated to expand at $\sim 1,000$ km/s (e.g., Porth et al. (2016), Reynolds et al. (2018), and Vorster et al. (2013)). Eq. (6) in Reynolds et al. (2018) gives the time it takes for an electron to lose half its energy via synchrotron radiation ($t_{1/2}$). For example, an electron that was emitting 12 keV photons $t_{1/2}$ years ago has cooled down by now to emit 3 keV photons ($\nu_{crit} \propto E^2$). Assuming that this electron traveled from the edge of the hard-band nebula ($\text{FWHM} = 15.2''$) to the edge of the soft-band nebula ($\text{FWHM} = 26.5''$) at velocity $v_{ad} = 1,000$ km/s, the constant average magnetic field inside the compact nebula yields $B = 24d_{3.5}^{-3/2} \mu\text{G}$. Compared with the $2.7 \mu\text{G}$ in the outer nebula, the much stronger magnetic field for the outer nebula was anticipated from the compact size of the hard X-ray inner nebula. This magnetic field estimate is consistent with the inner nebula magnetic field estimated by Van Etten et al. (2008) ($\sim 20 \mu\text{G}$ assuming a dipolar field) and Jin et al. (2023) ($\sim 22 \mu\text{G}$ assuming equipartition between the magnetic field and particle energy).

6. SUMMARY

As part of our *NuSTAR* observational campaign of energetic PWNe, we studied the X-ray properties of the Dragonfly PWN and its viability as a leptonic PeVatron. Our *NuSTAR* observation detected a compact ($r = 1'$) inner nebula of the Dragonfly in 3–20 keV. The size of this nebula decreases at higher energies, indicating synchrotron burnoff in a strong ($\sim 24 \mu\text{G}$) magnetic field near its pulsar PSR J2021+3651. The large diffuse outer nebula of the Dragonfly is observed in soft X-ray ($\sim 10'$) and radio ($\sim 2'$). We used these outer nebula spectra along with the TeV spectrum of eHWC J2019+368 to model the MW SED of the Dragonfly. The dynamical model yields the maximum particle energy of 1.4 PeV, and a low magnetic field ($2.7 \mu\text{G}$) averaged over the outer nebula in contrast to the high magnetic field in the inner nebula. At a nominal distance of 3.5 kpc, this 16-kyr-old PWN was found to have collided with the SNR reverse shock 4 kyrs ago. The highly asymmetric and energy-dependent morphology of the Dragonfly implies a fast proper motion of its pulsar ($\sim 1,000$ km/s) and/or inhomogeneity in the ISM that initiated an asymmetric

SNR – PWN interaction. Our future work will investigate these scenarios and provide a deeper understanding of particle transport in such an evolved system using radio, X-ray, and gamma-ray observations.

The Dragonfly shares common features with other PWNe in our *NuSTAR* observational campaigns with the maximum particle energies above 1 PeV – the Eel (Burgess et al. (2022)) and Boomerang (Pope et al. submitted to ApJ). These features include a compact hard X-ray inner nebula undergoing synchrotron burnoff, a large diffuse outer nebula in lower energy, and an absence of a GeV nebula. Opposite patterns are observed in two of our target PWNe, the K3 (Park et al. (2023b)) and Rabbit (Park et al. (2023a)). These PWNe exhibit extended hard X-ray nebulae without a sign of synchrotron burnoff, energy-insensitive morphologies, and bright GeV nebulae. The best-fit multi-zone models of the two PWNe yield the maximum particle energies below 1 PeV, while the PWNe are invisible to the current UHE observatories. The next-generation UHE observatories in the southern hemisphere (SWG0 and CTAO–South) will enable us to study the true energetics of the PWNe and its relation to the MW observations.

We thank Mattia Di Mauro for providing the GeV upper limits. We acknowledge Ruoyu Shang, Eric Gotthelf, and Jordan Eagle for their helpful discussions. We thank the referee for carefully reading our manuscript and providing valuable comments. Support for this work was partially provided by NASA through *NuSTAR* Cycle 6 Guest Observer Program grant NNH19ZDA001N. HA acknowledges support from the National Research Foundation of Korea (NRF) grant funded by the Korean Government (MSIT) (NRF-2023R1A2C1002718).

Facilities: *NuSTAR*, *Chandra*, XMM-Newton, *Fermi*-LAT

Software: NuSTARDAS (v2.0.0), CIAO (4.13; Fruscione et al. (2006)), SAS (v20.0.0; Gabriel et al. (2004)), Fermipy (v1.0.1; Wood et al. (2017)), HEASoft (Nasa High Energy Astrophysics Science Archive Research Center (Heasarc) (2014)), HENDRICS (7.0; Bachetti (2018)), Stingray (v1.1; Huppenkothen et al. (2019)), Xspec (Arnaud (1996)), Naima (Zabalza (2015))

REFERENCES

- Abdo, A. A., Allen, B., Berley, D., et al. 2007, ApJL, 658, L33, doi: [10.1086/513696](https://doi.org/10.1086/513696)
- Abdo, A. A., Ackermann, M., Ajello, M., et al. 2009, The Astrophysical Journal, 700, 1059, doi: [10.1088/0004-637x/700/2/1059](https://doi.org/10.1088/0004-637x/700/2/1059)
- Abeysekara, A. U., Archer, A., Aune, T., et al. 2018, The Astrophysical Journal, 861, 134, doi: [10.3847/1538-4357/aac4a2](https://doi.org/10.3847/1538-4357/aac4a2)
- Abeysekara, A. U., Albert, A., Alfaro, R., et al. 2020, Phys. Rev. Lett., 124, 021102, doi: [10.1103/PhysRevLett.124.021102](https://doi.org/10.1103/PhysRevLett.124.021102)
- Acero, F., Ackermann, M., Ajello, M., et al. 2013, ApJ, 773, 77, doi: [10.1088/0004-637x/773/1/77](https://doi.org/10.1088/0004-637x/773/1/77)
- Aharonian, F., An, Q., Axikegu, et al. 2021, Phys. Rev. Lett., 126, 241103, doi: [10.1103/PhysRevLett.126.241103](https://doi.org/10.1103/PhysRevLett.126.241103)
- Albert, A., Alfaro, R., Alvarez, C., et al. 2021, ApJ, 911, 143, doi: [10.3847/1538-4357/abecda](https://doi.org/10.3847/1538-4357/abecda)
- Aliu, E., Aune, T., Behera, B., et al. 2014, ApJ, 788, 78, doi: [10.1088/0004-637x/788/1/78](https://doi.org/10.1088/0004-637x/788/1/78)
- Arnaud, K. A. 1996, in Astronomical Society of the Pacific Conference Series, Vol. 101, Astronomical Data Analysis Software and Systems V, ed. G. H. Jacoby & J. Barnes, 17
- Bachetti, M. 2018, HENDRICS: High ENergy Data Reduction Interface from the Command Shell, Astrophysics Source Code Library, record ascl:1805.019, <http://ascl.net/1805.019>
- Ballet, J., Burnett, T. H., Digel, S. W., & Lott, B. 2020, Fermi Large Area Telescope Fourth Source Catalog Data Release 2, arXiv, doi: [10.48550/ARXIV.2005.11208](https://doi.org/10.48550/ARXIV.2005.11208)
- Barkov, M. V., Lyutikov, M., Klingler, N., & Bordas, P. 2019, MNRAS, 485, 2041, doi: [10.1093/mnras/stz521](https://doi.org/10.1093/mnras/stz521)
- Burgess, D. A., Mori, K., Gelfand, J. D., et al. 2022, The Astrophysical Journal, 930, 148, doi: [10.3847/1538-4357/ac650a](https://doi.org/10.3847/1538-4357/ac650a)
- Cao, Z., Aharonian, F. A., An, Q., et al. 2021a, Nature, 594, 33, doi: [10.1038/s41586-021-03498-z](https://doi.org/10.1038/s41586-021-03498-z)
- Cao, Z., Aharonian, F., An, Q., et al. 2021b, ApJL, 917, L4, doi: [10.3847/2041-8213/ac0fd5](https://doi.org/10.3847/2041-8213/ac0fd5)
- Collaboration, G., Vallenari, A., Brown, A., & et al., T. P. 2022, Astronomy & Astrophysics, doi: [10.1051/0004-6361/202243940](https://doi.org/10.1051/0004-6361/202243940)
- Cummings, A. C., Stone, E. C., Heikkilä, B. C., et al. 2016, The Astrophysical Journal, 831, 18, doi: [10.3847/0004-637x/831/1/18](https://doi.org/10.3847/0004-637x/831/1/18)
- De Luca, A., & Molendi, S. 2004, A&A, 419, 837, doi: [10.1051/0004-6361:20034421](https://doi.org/10.1051/0004-6361:20034421)

- Deharveng, L., Lefloch, B., Zavagno, A., et al. 2003, *A&A*, 408, L25, doi: [10.1051/0004-6361:20031157](https://doi.org/10.1051/0004-6361:20031157)
- Di Mauro, M., Manconi, S., Negro, M., & Donato, F. 2021, *Phys. Rev. D*, 104, 103002, doi: [10.1103/PhysRevD.104.103002](https://doi.org/10.1103/PhysRevD.104.103002)
- Dwarkadas, V. V. 2005, *The Astrophysical Journal*, 630, 892, doi: [10.1086/432109](https://doi.org/10.1086/432109)
- Fang, J., Wen, L., Yu, H., & Chen, S. 2020, *MNRAS*, 498, 4901, doi: [10.1093/mnras/staa2703](https://doi.org/10.1093/mnras/staa2703)
- Fang, K., Kerr, M., Blandford, R., Fleischhack, H., & Charles, E. 2022, *Phys. Rev. Lett.*, 129, 071101, doi: [10.1103/PhysRevLett.129.071101](https://doi.org/10.1103/PhysRevLett.129.071101)
- Fermi-LAT collaboration, :, Abdollahi, S., et al. 2022, arXiv e-prints, arXiv:2201.11184, <https://arxiv.org/abs/2201.11184>
- Freeman, P., Doe, S., & Siemiginowska, A. 2001, in *Society of Photo-Optical Instrumentation Engineers (SPIE) Conference Series*, Vol. 4477, *Astronomical Data Analysis*, ed. J.-L. Starck & F. D. Murtagh, 76–87, doi: [10.1117/12.447161](https://doi.org/10.1117/12.447161)
- Fruscione, A., McDowell, J. C., Allen, G. E., et al. 2006, in *Society of Photo-Optical Instrumentation Engineers (SPIE) Conference Series*, Vol. 6270, *Observatory Operations: Strategies, Processes, and Systems*, ed. D. R. Silva & R. E. Doxsey, 62701V, doi: [10.1117/12.671760](https://doi.org/10.1117/12.671760)
- Gabriel, C., Denby, M., Fyfe, D. J., et al. 2004, in *Astronomical Society of the Pacific Conference Series*, Vol. 314, *Astronomical Data Analysis Software and Systems (ADASS) XIII*, ed. F. Ochsenbein, M. G. Allen, & D. Egret, 759
- Gaensler, B. M., & Slane, P. O. 2006, *Annual Review of Astronomy and Astrophysics*, 44, 17, doi: [10.1146/annurev.astro.44.051905.092528](https://doi.org/10.1146/annurev.astro.44.051905.092528)
- Gelfand, J. D., Slane, P. O., & Zhang, W. 2009, *The Astrophysical Journal*, 703, 2051, doi: [10.1088/0004-637x/703/2/2051](https://doi.org/10.1088/0004-637x/703/2/2051)
- Gotthelf, E. V., Mori, K., Aliu, E., et al. 2016, *The Astrophysical Journal*, 826, 25, doi: [10.3847/0004-637x/826/1/25](https://doi.org/10.3847/0004-637x/826/1/25)
- Halpern, J. P., Camilo, F., Giuliani, A., et al. 2008, *The Astrophysical Journal*, 688, L33, doi: [10.1086/594117](https://doi.org/10.1086/594117)
- Hartman, R. C., Bertsch, D. L., Bloom, S. D., et al. 1999, *ApJS*, 123, 79, doi: [10.1086/313231](https://doi.org/10.1086/313231)
- H.E.S.S. Collaboration, Abdalla, H., Abramowski, A., et al. 2018, *A&A*, 612, A2, doi: [10.1051/0004-6361/201629377](https://doi.org/10.1051/0004-6361/201629377)
- Hessels, J. W. T., Roberts, M. S. E., Ransom, S. M., et al. 2004, *ApJ*, 612, 389, doi: [10.1086/422408](https://doi.org/10.1086/422408)
- Huppenkothen, D., Bachetti, M., Stevens, A. L., et al. 2019, *ApJ*, 881, 39, doi: [10.3847/1538-4357/ab258d](https://doi.org/10.3847/1538-4357/ab258d)
- Jansson, R., & Farrar, G. R. 2012, *ApJ*, 757, 14, doi: [10.1088/0004-637X/757/1/14](https://doi.org/10.1088/0004-637X/757/1/14)
- Jin, R., Ng, C.-Y., Roberts, M. S. E., & Li, K.-L. 2023, *The Astrophysical Journal*, 942, 100, doi: [10.3847/1538-4357/aca656](https://doi.org/10.3847/1538-4357/aca656)
- Kargaltsev, O., Pavlov, G. G., Klingler, N., & Rangelov, B. 2017, *Journal of Plasma Physics*, 83, 635830501, doi: [10.1017/S0022377817000630](https://doi.org/10.1017/S0022377817000630)
- Kargaltsev, O., Rangelov, B., & Pavlov, G. G. 2013, *Gamma-ray and X-ray Properties of Pulsar Wind Nebulae and Unidentified Galactic TeV Sources*, <https://arxiv.org/abs/1305.2552>
- Kirichenko, A., Danilenko, A., Shternin, P., et al. 2015, *The Astrophysical Journal*, 802, 17, doi: [10.1088/0004-637x/802/1/17](https://doi.org/10.1088/0004-637x/802/1/17)
- Kolb, C., Blondin, J., Slane, P., & Temim, T. 2017, *ApJ*, 844, 1, doi: [10.3847/1538-4357/aa75ce](https://doi.org/10.3847/1538-4357/aa75ce)
- Law, D. R., DeGioia-Eastwood, K., & Moore, K. L. 2002, *ApJ*, 565, 1239, doi: [10.1086/337922](https://doi.org/10.1086/337922)
- Mizuno, T., Tanaka, N., Takahashi, H., et al. 2017, *The Astrophysical Journal*, 841, 104, doi: [10.3847/1538-4357/aa7201](https://doi.org/10.3847/1538-4357/aa7201)
- Mori, K., An, H., Burgess, D., et al. 2022, in 37th International Cosmic Ray Conference, 963, doi: [10.22323/1.395.0963](https://doi.org/10.22323/1.395.0963)
- Nasa High Energy Astrophysics Science Archive Research Center (Heasarc). 2014, HEASoft: Unified Release of FTOOLS and XANADU, Astrophysics Source Code Library, record ascl:1408.004. <http://ascl.net/1408.004>
- Ohira, Y., Kisaka, S., & Yamazaki, R. 2018, *Monthly Notices of the Royal Astronomical Society*, 478, 926, doi: [10.1093/mnras/sty1159](https://doi.org/10.1093/mnras/sty1159)
- Paredes, J. M., Martí, J., Ishwara-Chandra, C. H., et al. 2009, *A&A*, 507, 241, doi: [10.1051/0004-6361/200912448](https://doi.org/10.1051/0004-6361/200912448)
- Park, J., Kim, C., Woo, J., et al. 2023a, *The Astrophysical Journal*, 945, 66, doi: [10.3847/1538-4357/acba0e](https://doi.org/10.3847/1538-4357/acba0e)
- . 2023b, *The Astrophysical Journal*, 945, 33, doi: [10.3847/1538-4357/acb1b0](https://doi.org/10.3847/1538-4357/acb1b0)
- Porth, O., Vorster, M. J., Lyutikov, M., & Engelbrecht, N. E. 2016, *Monthly Notices of the Royal Astronomical Society*, 460, 4135, doi: [10.1093/mnras/stw1152](https://doi.org/10.1093/mnras/stw1152)
- Reynolds, S. P., Borkowski, K. J., & Gwynne, P. H. 2018, *ApJ*, 856, 133, doi: [10.3847/1538-4357/aab3d3](https://doi.org/10.3847/1538-4357/aab3d3)
- Roberts, M. S. E., Hessels, J. W. T., Ransom, S. M., et al. 2002, *ApJL*, 577, L19, doi: [10.1086/344082](https://doi.org/10.1086/344082)
- Roberts, M. S. E., Romani, R. W., & Kawai, N. 2001, *The Astrophysical Journal Supplement Series*, 133, 451, doi: [10.1086/320352](https://doi.org/10.1086/320352)

- Roberts, M. S. E., Brogan, C., Ransom, S., et al. 2008, in American Institute of Physics Conference Series, Vol. 1085, American Institute of Physics Conference Series, ed. F. A. Aharonian, W. Hofmann, & F. Rieger, 328–331, doi: [10.1063/1.3076673](https://doi.org/10.1063/1.3076673)
- Rodón, J. A., Zavagno, A., Baluteau, J. P., et al. 2010, A&A, 518, L80, doi: [10.1051/0004-6361/201014609](https://doi.org/10.1051/0004-6361/201014609)
- Sudoh, T., Linden, T., & Hooper, D. 2021, Journal of Cosmology and Astroparticle Physics, 2021, 010, doi: [10.1088/1475-7516/2021/08/010](https://doi.org/10.1088/1475-7516/2021/08/010)
- Tang, X., & Chevalier, R. A. 2012, The Astrophysical Journal, 752, 83, doi: [10.1088/0004-637X/752/2/83](https://doi.org/10.1088/0004-637X/752/2/83)
- Temim, T., Slane, P., Kolb, C., et al. 2015, ApJ, 808, 100, doi: [10.1088/0004-637X/808/1/100](https://doi.org/10.1088/0004-637X/808/1/100)
- Temim, T., Slane, P., Plucinsky, P. P., et al. 2017, The Astrophysical Journal, 851, 128, doi: [10.3847/1538-4357/aa9d41](https://doi.org/10.3847/1538-4357/aa9d41)
- Toalá, J. A., Guerrero, M. A., Chu, Y.-H., et al. 2012, The Astrophysical Journal, 755, 77, doi: [10.1088/0004-637X/755/1/77](https://doi.org/10.1088/0004-637X/755/1/77)
- Torres, D. F., ed. 2017, Modelling Pulsar Wind Nebulae (Springer International Publishing), doi: [10.1007/978-3-319-63031-1](https://doi.org/10.1007/978-3-319-63031-1)
- Van Etten, A., Romani, R. W., & Ng, C. Y. 2008, ApJ, 680, 1417, doi: [10.1086/587865](https://doi.org/10.1086/587865)
- Verbunt, F., Igoshev, A., & Cator, E. 2017, A&A, 608, A57, doi: [10.1051/0004-6361/201731518](https://doi.org/10.1051/0004-6361/201731518)
- Vorster, M. J., Tibolla, O., Ferreira, S. E. S., & Kaufmann, S. 2013, The Astrophysical Journal, 773, 139, doi: [10.1088/0004-637X/773/2/139](https://doi.org/10.1088/0004-637X/773/2/139)
- Weaver, R., McCray, R., Castor, J., Shapiro, P., & Moore, R. 1977, ApJ, 218, 377, doi: [10.1086/155692](https://doi.org/10.1086/155692)
- Wilms, J., Allen, A., & McCray, R. 2000, ApJ, 542, 914, doi: [10.1086/317016](https://doi.org/10.1086/317016)
- Wood, M., Caputo, R., Charles, E., et al. 2017, in International Cosmic Ray Conference, Vol. 301, 35th International Cosmic Ray Conference (ICRC2017), 824. <https://arxiv.org/abs/1707.09551>
- Xu, J.-L., Xu, Y., Yu, N., et al. 2017, The Astrophysical Journal, 849, 140, doi: [10.3847/1538-4357/aa8ee0](https://doi.org/10.3847/1538-4357/aa8ee0)
- Zabalza, V. 2015, Proc. of International Cosmic Ray Conference 2015, 922
- Zabalza, V., Paredes, J. M., Martí, J., Sánchez-Sutil, J. R., & Muñoz-Arjonilla, A. J. 2010, in Astronomical Society of the Pacific Conference Series, Vol. 422, High Energy Phenomena in Massive Stars, ed. J. Martí, P. L. Luque-Escamilla, & J. A. Combi, 186